Silicic volcanism on Mars evidenced by tridymite in high-SiO$_2$ sedimentary rock at Gale crater

Richard V. Morris[a,1], David T. Vaniman[b], David F. Blake[c], Ralf Gellert[d], Steve J. Chipera[e], Elizabeth B. Rampe[f], Douglas W. Ming[a], Shaunna M. Morrison[g], Robert T. Downs[g], Allan H. Treiman[h], Albert S. Yen[i], John P. Grotzinger[j,1], Cherie N. Achilles[g], Thomas F. Bristow[c], Joy A. Crisp[i], David J. Des Marais[c], Jack D. Farmer[k], Kim V. Fendrich[g], Jens Frydenvang[l,m], Trevor G. Graff[n], John-Michael Morookian[i], Edward M. Stolper[j], and Susanne P. Schwenzer[h,o]

[a]NASA Johnson Space Center, Houston, TX 77058; [b]Planetary Science Institute, Tucson, AZ 85719; [c]NASA Ames Research Center, Moffitt Field, CA 94035; [d]Department of Physics, University of Guelph, Guelph, ON, Canada N1G 2W1; [e]Chesapeake Energy, Oklahoma City, OK 73118; [f]Aerodyne Industries, Houston, TX 77058; [g]Department of Geosciences, University of Arizona, Tucson, AZ 85721; [h]Lunar and Planetary Institute, Houston, TX 77058; [i]Jet Propulsion Laboratory, California Institute of Technology, Pasadena, CA 91109; [j]Division of Geological and Planetary Sciences, California Institute of Technology, Pasadena, CA 91125; [k]School of Earth and Space Exploration, Arizona State University, Tempe, AZ 85287; [l]Los Alamos National Laboratory, Los Alamos, NM 87545; [m]Niels Bohr Institute, University of Copenhagen, 2100 Copenhagen, Denmark; [n]Jacobs, Houston, TX 77058; and [o]Department of Environment, Earth and Ecosystems, The Open University, Milton Keynes MK7 6AA, United Kingdom

Tridymite, a low-pressure, high-temperature (>870 °C) SiO$_2$ polymorph, was detected in a drill sample of laminated mudstone (Buckskin) at Marias Pass in Gale crater, Mars, by the Chemistry and Mineralogy X-ray diffraction instrument onboard the Mars Science Laboratory rover *Curiosity*. The tridymitic mudstone has ~40 wt.% crystalline and ~60 wt.% X-ray amorphous material and a bulk composition with ~74 wt.% SiO$_2$ (Alpha Particle X-Ray Spectrometer analysis). Plagioclase (~17 wt.% of bulk sample), tridymite (~14 wt.%), sanidine (~3 wt.%), cation-deficient magnetite (~3 wt.%), cristobalite (~2 wt.%), and anhydrite (~1 wt.%) are the mudstone crystalline minerals. Amorphous material is silica-rich (~39 wt.% opal-A and/or high-SiO$_2$ glass and opal-CT), volatile-bearing (16 wt.% mixed cation sulfates, phosphates, and chlorides−perchlorates−chlorates), and has minor TiO$_2$ and Fe$_2$O$_3$T oxides (~5 wt.%). Rietveld refinement yielded a monoclinic structural model for a well-crystalline tridymite, consistent with high formation temperatures. Terrestrial tridymite is commonly associated with silicic volcanism, and detritus from such volcanism in a "Lake Gale" catchment environment can account for Buckskin's tridymite, cristobalite, feldspar, and any residual high-SiO$_2$ glass. These cogenetic detrital phases are possibly sourced from the Gale crater wall/rim/central peak. Opaline silica could form during diagenesis from high-SiO$_2$ glass, as amorphous precipitated silica, or as a residue of acidic leaching in the sediment source region or at Marias Pass. The amorphous mixed-cation salts and oxides and possibly the crystalline magnetite (otherwise detrital) are primary precipitates and/or their diagenesis products derived from multiple infiltrations of aqueous solutions having variable compositions, temperatures, and acidities. Anhydrite is post lithification fracture/vein fill.

Mars | tridymite | Gale crater | lake | volcanism

The Mars Science Laboratory (MSL) rover, *Curiosity*, has been exploring sedimentary rocks within Gale crater since landing in August 2012, and progressing upward through a sequence of strata exposed along the lower slopes of Aeolis Mons (informally known as Mount Sharp). This traverse has taken *Curiosity* through sequences of fluvial, deltaic, and lacustrine sediments (e.g., ref. 1). On sol 1057 (the number of martian days since landing), *Curiosity* began preparations for collecting drill powder from high-silica sedimentary rock at a location named Buckskin. We describe the geologic setting of the Buckskin sample location, the detection of significant amounts of the silica polymorph tridymite by the MSL Chemistry and Mineralogy (CheMin) X-ray diffraction instrument, and its implications for volcanism on Mars.

Geologic Setting

The Buckskin outcrop is part of the Murray formation of lacustrine mudstones exposed in the Marias Pass area (*SI Appendix*, Figs. S1 and S2). The formation was previously studied in the Pahrump Hills

(1), where three drill samples were analyzed by CheMin [Confidence Hills, Mojave2, and Telegraph Peak (2)]. With the assumption that bedding is approximately horizontal, the Marias Pass outcrop is ~2–3 m thick and ~6 m higher in stratigraphic position than the highest outcrop sampled in the Pahrump Hills (Telegraph Peak) (1). Mudstone, generally characterized by fine lamination, is the dominant depositional facies in the Pahrump Hills (1) and also at Marias Pass, as shown by the Mars Hand Lens Imager images of Marias Pass bedrock and the dust-free float rock Lamoose (Fig. 1*A*). Here the laminae have a mean thickness of ~0.5 mm and are characteristically parallel; individual laminae are laterally continuous for at least several tens of centimeters. The mudstone facies lacks evidence for cross-stratification at any scale, sediment

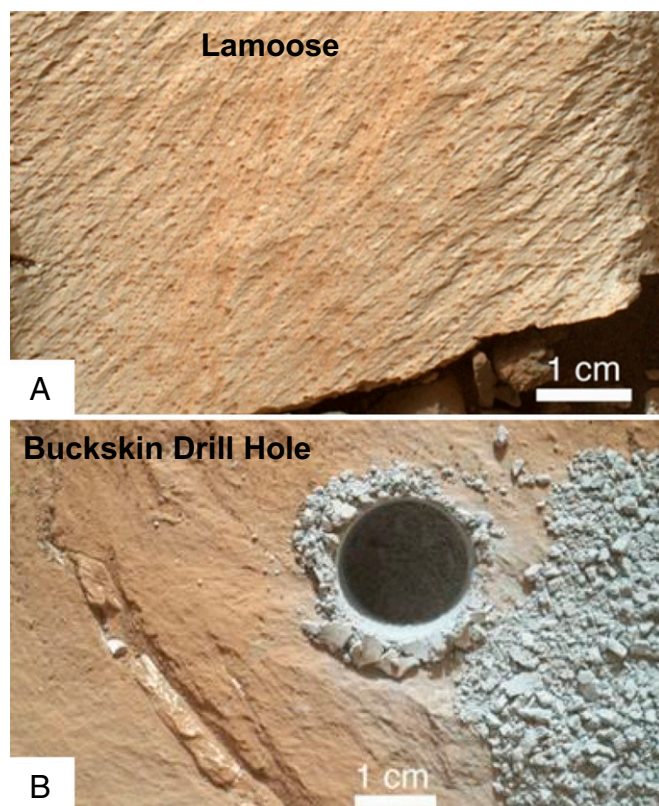EARTH, ATMOSPHERIC, AND PLANETARY SCIENCES

Fig. 1. (*A*) Lamoose is a float block of Murray formation, rotated and eroded by wind to reveal very fine lamination in addition to fine grain size. Wind-induced surface striations trend obliquely to primary depositional lamination. (*B*) The Buckskin drill hole penetrates tridymitic mudstone of the Murray formation at Marias Pass. Image courtesy of NASA/JPL-Caltech/MSSS.

transport (or erosion) by traction currents, sediment-filled mud-cracks, intraclasts that indicate reworking of mud by currents, or clasts. The observed features are characteristic of lacustrine sedimentation and contrast strongly with subaerial settings associated with eolian, fluvial, volcanic, or impact processes (1).

Table 1. Composition of presieve and postsieve dump piles (from APXS) and calculated compositions of crystalline and amorphous materials

	Presieve, wt.%	Postsieve, wt.%	Crystalline,* wt.%	Amorphous,* wt.%
SiO_2	74.43	73.65	68.20	77.01
TiO_2	1.66	1.57	0.12	2.54
Al_2O_3	5.45	5.66	13.91	0.04
Cr_2O_3	0.08	0.10	0.00	0.17
FeOT	4.94	5.49	7.27	4.71
MnO	0.08	0.09	0.00	0.15
MgO	0.72	0.82	0.16	1.26
CaO	2.99	3.05	5.25	1.54
Na_2O	2.01	2.08	2.80	1.58
K_2O	0.99	0.96	1.35	0.69
P_2O_5	1.29	1.25	0.00	2.09
SO_3	4.85	4.80	1.06	7.31
Cl	0.28	0.29	0.00	0.49
Total	99.77	99.81	100.12	99.60

*Amorphous material composition calculated using APXS postsieve dump pile analysis as bulk composition, 40 wt.% crystalline material, and 60 wt.% amorphous material.

Buckskin Mineralogical Composition

Targets for chemical analyses by the Alpha Particle X-Ray Spectrometer (APXS) at the Buckskin site included tailings from the test drill hole (sol 1059), the sample acquisition hole (sol 1064; Fig. 1*B*), and dump piles from emptying the Collection and Handling for In-Situ Martian Rock Analysis tool before (sol 1065) and after (sol 1091) the collected drill powder was sieved to <150 μm [see MSL mission overview for background (3)]. The chemical similarity of APXS analyses of the presieve and postsieve dump piles (Table 1) indicates that mineralogical fractionation between bulk sample and CheMin-analyzed sample (<150-μm postsieve dump pile) is minimal.

CheMin is a transmission X-ray diffraction (XRD) and X-ray fluorescence instrument that uses cobalt radiation to produce two-dimensional Co Kα diffraction images (Debye ring pattern) (4). Samples are normally measured over the course of three nights, producing 45 total images that are summed and converted to a one-dimensional diffraction pattern over an angular range of 2–52° 2θ. The diffraction pattern used for Buckskin quantitative XRD analysis was the sum of the first 4 of 45 diffraction images, and tridymite peaks are clearly evident (Fig. 2). The remaining 41 images are affected by on-ring and off-ring diffraction spots. Coincident with the appearance of abundant spots are a decrease in the intensities of tridymite diffraction peaks (by ~50%) and a concomitant increase in the intensities of anhydrite diffraction peaks. This observation is based on a comparison of diffraction patterns for the sum of images 1 through 4 and 16 through 45, with each normalized to 45 images (i.e., the same integration time) (*SI Appendix*, Fig. S3). The explanation for the change in the nature of the diffraction patterns after image 4, possibly resulting from poor grain motion and particle clumping, is under investigation.

For quantitative analysis of CheMin XRD data, we used the full pattern-fitting capability (Rietveld) in JADE (Materials Data Inc.), with refinement of literature cell parameters (5) for well-crystalline minerals present at >5 wt.% abundance, and FULLPAT analysis for poorly crystalline and XRD-amorphous phases (6–9). The combined results from both analyses are listed in Table 2. Unit cell parameters were refined for tridymite, plagioclase, sanidine, and magnetite (Table 3). The two most abundant crystalline minerals are plagioclase (43 wt.% of crystalline material; ~An_{41}) and tridymite (34 wt.%). All tridymite principal diffraction intensities (10) are present and well defined at instrument resolution (Table 4 and Fig. 2). They are indicative of fully ordered monoclinic tridymite, originally formed at high temperatures, as opposed to a disordered material like opal-CT, which has broad diffraction peaks that represent portions of a disordered tridymite structure in the 4.05–4.10 Å and 2.50 Å regions and with a weak diffraction peak at 4.25–4.35 Å (11). There are suggestions in the literature that opal-T can exist as a substance more ordered toward tridymite than opal-CT, which would be recognized by a broad diffraction peak near 4.107 Å and weaker broad diffraction peaks near 4.328 Å and 2.50 Å (12). However, the Buckskin tridymite shows none of these characteristics. Refined diffraction patterns for plagioclase, tridymite, sanidine, and magnetite are illustrated in *SI Appendix*, Fig. S4, as well as patterns of cristobalite and anhydrite whose unit cell parameters were fixed during refinement.

The poorly crystalline or XRD amorphous material was modeled by contributions from opal-A, obsidian, and opal-CT to account for the diffuse diffraction feature centered near 26° 2θ and a low-angle scattering component that also includes a diffuse ferrihydrite-like diffraction feature centered near 40° 2θ (*SI Appendix*, Fig. S5). Instrumental artifacts, including a peak near 6.6° 2θ (~15 Å) from the Kapton cell window, were modeled using CheMin patterns from analyses of empty cells with Kapton windows. Although opal-A was used to model the amorphous material, any high-SiO_2 phase with a similar XRD pattern can be used, including SiO_2 glass, gem opal, and silica gel. (See *SI Appendix*, Fig. S6 for XRD patterns of amorphous high-SiO_2 materials produced by synthetic and natural
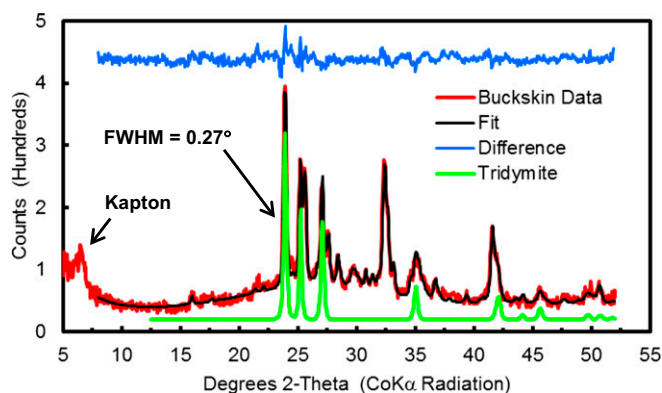
Fig. 2. Buckskin diffraction pattern (red) from sum of first four diffraction images, calculated pattern from Rietveld analysis (black), difference pattern (blue), and refined tridymite pattern (offset green); see *SI Appendix*, Fig. S4 for refined patterns of all minerals. Full width at half maximum intensity (FWHM) of the tridymite peak at 23.9° 2θ is 0.27° 2θ, which corresponds to CheMin 2θ resolution measured on Earth before launch (ref. 4, figure 18). Peak at ~6.5° 2θ is from the Kapton cell window.

processes.) The amount of amorphous material in the bulk sample based on FULLPAT is 50 ± 15 wt.% (Table 2).

Chemistry of Crystalline and Amorphous Materials

The chemical compositions of Buckskin plagioclase, tridymite, sanidine, and magnetite were estimated from unit cell parameters calculated by Rietveld refinement (Table 3). However, mineral unit cell parameters are insensitive to abundances of trace and minor elements (e.g., Fe in plagioclase). To limit artificial assignments of these elements to the amorphous material, we adopted compositions of naturally occurring materials for the chemical compositions of plagioclase, tridymite, and sanidine (13–15), subject to the constraint that their compositions are consistent with those derived from XRD unit cell parameters (Table 3 and *SI Appendix*, Table S1). This approach was more difficult for magnetite, because its refined cell ($a = 8.359 \pm 0.001$ Å; Table 3) is too small for stoichiometric magnetite [Fe_3O_4; $a = 8.394$ Å (5)]. The cell parameters and bulk rock composition are most consistent with cation-deficient magnetite ($Fe_{2.78}O_4$) to accommodate the observed magnetite unit cell parameters. Alternatives to reduce the magnetite unit cell parameters that are not reasonable based on the bulk composition of the rock (Table 1) include a chromite [$Fe^{2+}(Cr,Fe^{3+})_2O_4$] component (too little Cr) and hercynite ($FeAl_2O_4$) or spinel ($MgAl_2O_4$) components (all Al is associated with feldspar). An ulvöspinel (Fe_2TiO_4) component gives a larger cell parameter rather than the smaller one observed. Stoichiometric compositions were used for cristobalite and anhydrite (*SI Appendix*, Table S1), and their unit cell parameters were fixed to literature values (5) during Rietveld analysis because these minerals were not present in sufficiently high concentrations (Table 3) to permit meaningful refinement of unit cell parameters.

The chemical composition of crystalline material in Buckskin (Table 1) was calculated from mineral chemical compositions (*SI Appendix*, Table S1) and their abundances (Table 2). The high SiO_2 concentration (~68 wt.%) in the crystalline material reflects the high relative proportion of tridymite and feldspars. The bulk composition of the Buckskin sample (Table 1), the composition of the crystalline component (Table 1), and the weight proportion of the amorphous material from FULLPAT (a relatively uncertain 50 ± 15 wt.%) enable calculation (by mass balance) of the chemical composition of the noncrystalline (i.e., XRD amorphous) material (Table 1). However, the value of 50 wt.% results in an amorphous material with a calculated negative Al_2O_3 concentration (~-2.6 wt.%), which is not physically possible. Increasing the abundance of the amorphous

material in the calculations results in a positive Al_2O_3 concentration (0.04 wt.%; Table 1) at 60 wt.%. We take this value, which is within the uncertainty limits of the FULLPAT value, to represent the proportion of amorphous material, recognizing that the value could be higher. The amorphous material has a calculated value of ~77 wt.% SiO_2, which is consistent with the observed broad diffraction hump centered near 26° 2θ that is expected for high-SiO_2 amorphous materials (*SI Appendix*, Fig. S6).

The calculated composition of the amorphous material also has a high anion concentration ($SO_3 + P_2O_5 + Cl$ ~10 wt.%) (Table 1). Charge balance in the amorphous material is achieved if these anions occur predominantly as mixed-cation sulfate, phosphate, and chloride−perchlorate−chlorate XRD-amorphous salts. This calculation excludes SiO_2 and TiO_2, which do not readily form salts, and results in a small oxide excess (~2 wt.%) taken as amorphous Fe_2O_3.

Tridymite Formation Pathways

Tridymite is the stable polymorph of SiO_2 at low pressures (up to ~0.4 GPa) between ~870 °C and ~1,470 °C (e.g., refs. 16 and 17) and is thus metastable under ambient terrestrial (and martian) surface conditions. It is readily produced under laboratory conditions within its stability field, especially with alkali fluxes (18–27). We are not aware of any geologically reasonable, low-temperature formation pathway for preparation of tridymite outside of its thermochemical stability field. In the following paragraphs, we focus on natural occurrences of tridymite and evaluate their applicability to the origin of abundant tridymite in the Buckskin sample. Unless otherwise noted, the tridymite crystal structure is unspecified in the cited references.

Many terrestrial tridymite occurrences are associated with silicic volcanism, which, by its nature, has the requisites of high temperatures and high-SiO_2 lava compositions (dacite and rhyolite) for tridymite formation within its stability field. Vapor-phase formation of tridymite (along with sanidine and iron oxides) occurs in vugs and lithophysae in rhyolitic ash-flow tuff (28–35). For example, the mineral stratigraphy within compound cooling units of a rhyolitic ash-flow tuff showed tridymite is most abundant (~25 wt.%) in the central zone where temperatures were highest and occurs along with sanidine as crystals growing into voids; cristobalite and sanidine occur in cooler zones where replacement of glass predominates (30). Tridymite derived from oxidation of fayalite has also been reported in a rhyolite flow (Oregon) (36). At the Iwodake rhyolitic cone of Satsuma-Iwojima volcano (Japan), a tridymite formation pathway is alteration of rhyolite by volcanic vapors and acidic hydrothermal fluids at temperatures up to 900 °C (37–40).

Table 2. Mineralogy of Buckskin drill sample relative to crystalline material and relative to bulk sample using XRD- and APXS-derived concentrations for the amorphous material

		Bulk sample	
	Crystalline material*	XRD*	APXS*
Plagioclase	42.8 ± 3.0	21.4 ± 1.5	17.1 ± 1.2
Sanidine	8.4 ± 1.8	4.2 ± 0.9	3.4 ± 0.7
Magnetite	6.9 ± 0.8	3.5 ± 0.4	2.8 ± 0.3
Anhydrite	1.8 ± 0.6	0.9 ± 0.3	0.7 ± 0.2
Tridymite	34.1 ± 2.0	17.1 ± 1.0	13.6 ± 0.8
Cristobalite	6.0 ± 0.8	3.0 ± 0.4	2.4 ± 0.3
Amorphous	—	$50 \pm 15^{†}$	$60^{†,‡}$
Total	100	100	100

*Units = wt.%; uncertainties are 2σ.
†Includes contributions from the broad hump centered near 26° 2θ [modeled as opal-A plus obsidian (33 wt.% of bulk sample) and opal-CT (6 wt.%)] and the broad hump centered near 40° 2θ modeled as ferrihydrite plus low-angle scattering (21 wt.%) (*SI Appendix*, Fig. S5).
‡Lower limit; constrained by APXS chemistry.

Table 3. Space groups, unit cell parameters, and compositions from Rietveld analysis

	Tridymite	Plagioclase	Sanidine	Magnetite
Space group	Cc	$C\bar{1}$	$C2/m$	$Fd\bar{3}m$
a, Å	4.996 ± 0.002	8.155 ± 0.006	8.54 ± 0.02	8.359 ± 0.002
b, Å	8.671 ± 0.005	12.862 ± 0.006	13.01 ± 0.02	8.359 ± 0.002
c, Å	8.194 ± 0.003	7.106 ± 0.004	7.15 ± 0.02	8.359 ± 0.002
α, deg	90	93.32 ± 0.03	90	90
β, deg	90.43 ± 0.02	116.28 ± 0.03	115.8 ± 0.1	90
γ, deg	90	90.10 ± 0.04	90	90
V, Å³	352.8 ± 0.3	666.9 ± 0.5	716 ± 3	584.04 ± 0.4

Tridymite and sanidine are monoclinic; plagioclase is triclinic; magnetite is cubic. Chemical compositions calculated from unit cell parameters are $An_{41 \pm 4}Ab_{59 \pm 4}$ (plagioclase), $Ab_{32 \pm 16}Or_{68 \pm 16}$ (sanidine), and $Fe_{2.78 \pm 0.05}O_4$ (cation-deficient magnetite). Uncertainties are 1σ.

Acid sulfate leaching of rhyolite also occurred there, increasing the SiO_2 concentration from ~71 wt.% to ~97 wt.%.

The temperature regime associated with basaltic and intermediate volcanism can also provide a formation pathway for tridymite when the requisite high-SiO_2 material is present. Pyroclastic flows and associated ash plumes generated by partial lava dome collapse at andesitic Soufriere Hills volcano (Montserrat) have 10–27 wt.% tridymite plus cristobalite with minor quartz in their <10-μm size fraction (41). The tridymite and cristobalite are inferred to have formed by vapor-phase crystallization and devitrification of rhyolitic glass (~78 wt.% SiO_2) within the lava dome. In altered basalts from Stromboli volcano (Aeolian Islands, Italy) and andesites from Augustine volcano (Alaska), the high-SiO_2 host for tridymite is the residue after acid sulfate leaching of primary mafic rock (42, 43). Pyrometamorphic ejecta (buchite) blocks (tridymite–clinopyroxene facies) have up to ~90 vol.% tridymite at Stromboli volcano. Occurrences of quartz paramorphs after tridymite have been reported in contact metamorphic assemblages between high-SiO_2 rocks and basaltic lava (e.g., refs. 44–46); however, quartz and not tridymite would be detected by CheMin for an equivalent assemblage at Gale crater. The high concentrations of tridymite (~14 wt.% of bulk sample) and SiO_2 (~74 wt.%) for the Buckskin sample are not reasonably sourced from low-silica volcanics for which tridymite concentrations would be very low when averaged over the volumetric equivalent of a "Lake Gale" catchment involving entirely basaltic to intermediate volcanics.

Tridymite has been reported at terrestrial impact structures where target lithologies are SiO_2-rich and heated to elevated temperatures by the impact event (47, 48). Monoclinic tridymite was reported (abundance not quantified) in a core from the Chesapeake Bay impact structure, but only in a silica-rich 5-cm interval (~70 wt.% SiO_2 relative to whole rock) (48). In cores from the Popigai impact structure (gneiss target lithology), we calculate from ref. 47 that the mean tridymite concentration of melt rocks is ~1 vol.%, although up to ~5 vol.% tridymite is reported for several individual melt rocks. The impact that created Gale crater (~150 km diameter) generated a melt pool possibly of 0.5–1 km thickness (49) and presumably injected impact melt into fractured crater walls and central uplift. Even if the preimpact target lithology were SiO_2-rich (an assumption implying silicic volcanism predating the Gale impact), the high tridymite concentration in the Buckskin laminated mudstones is unlikely sourced from a Lake Gale catchment of impact melt rocks given the low tridymite abundance of known impactites.

As with terrestrial occurrences, tridymite in extraterrestrial samples has also been inferred to result from high-temperature igneous and/or impact processes on parent bodies or to form by direct condensation at high temperatures in the solar nebulae (e.g., refs. 24 and 50–58). Tridymite, cristobalite, quartz, and/or silica-rich glass are reported as minor constituents of lunar samples (e.g., ref. 57) and martian meteorites (e.g., refs. 51, 53, and 59). A granitic microclast in polymict ureilite EET 87720 contains a phase tentatively identified as tridymite by micro-XRD, with ~98 wt.% SiO_2 (58). The bulk composition of

the microclast (excluding interstitial glass) has ~77 wt.% SiO_2, and the interstitial glass is silica-rich (SiO_2 ~73 wt.%) and volatile-rich (~11 wt.% SO_3 and ~1 wt.% Cl). According to ref. 58, this microclast is evidence for an evolved melt on an unknown parent body with isotopic and volatile element data possibly pointing to Mars.

Tridymite has been synthesized in the laboratory by heating amorphous SiO_2 at 196 °C in glycol solutions (60). Aside from the fact that the chemical composition of the solutions used in these experiments is not geologically realistic, the temperature of the experiments is higher than those inferred so far for diagenesis at Gale crater [<~80 °C (8)], and the relative intensities of the diffraction peaks for the tridymite synthesized by ref. 60 differ markedly from those for the well-crystalline Buckskin tridymite (Table 4). These experiments indicate that low-temperature synthesis of metastable tridymite is possible and should be further explored. The apparent absence in nature of tridymite formation at low temperatures, based on studies of terrestrial and extraterrestrial rocks over many years (61–72) (see *SI Appendix*), suggests that this is an unlikely explanation for the large quantities of tridymite observed in the Buckskin sample.

Significance of Tridymite in the Murray Formation

In the absence of a geologically credible, low-temperature formation pathway for tridymite, and based on the consistency of its occurrences in natural samples as discussed in *Tridymite Formation Pathways*, we infer that tridymite in the Murray formation (Buckskin drill sample)

Table 4. Peak intensities and lattice d-spacings of refined tridymite in Buckskin sample compared with monoclinic Cc tridymite (10)

hkl*	Intensity		d, Å	
	Ref. 10	Buckskin	Ref. 10	Buckskin
110	100	100	4.3260	4.3222
020	45.9	46.2	4.3002	4.3060
002	75.9	75.6	4.1070	4.0972
−111	29.7	29.0	3.8641	3.8276
021	28.6	28.7	3.8097	3.8118
111	23.5	23.9	3.7921	3.8184
−112	10.9	10.6	3.0130	2.9779
022	13.5	13.4	2.9701	2.9682
112	7.3	7.6	2.9452	2.9692
200	10.8	11.2	2.5026	2.4986
130	17.7	17.2	2.4877	2.4892
−131	2.9	3.1	2.3896	2.3828
−113	2.8	2.9	2.3378	2.3121
023	3.9	3.8	2.3096	2.3066
113	6.7	6.8	2.2901	2.3060

*hkl are the Miller indices.

is a marker for low-pressure and high-temperature (>870 °C) processes, consistent with its stability field, and high-SiO_2 precursor lithologies. Silicic volcanism fits the geologic, thermal, and mineralogical context best, with tridymite being incorporated into the Murray formation laminated mudstone (i.e., tridymitic mudstone) at Buckskin as detrital sediment from erosion of silicic volcanic rocks. It follows that, if cogenetic, the cristobalite, sanidine, plagioclase, and any amorphous high-SiO_2 glass are also detrital. The high-SiO_2 glass would constitute some unknown fraction of the amorphous silica material determined by CheMin (33 wt.% of bulk as opal-A and/or high-SiO_2 glass). However, we infer, from the presence of opal-CT in the Buckskin amorphous material, that any glass has undergone diagenesis at least in part if not wholly to opal-A and opal-CT. This diagenesis could have occurred in the volcanic source area or subsequent to lithification of tridymitic mudstone at Marias Pass. If the diagenesis took place in the source region, the opaline material is detrital.

Lacustrine sediments in cores from Lake Tecocomulco (Mexico), with a catchment basin that includes basaltic−andesitic, andesitic, and rhyolitic volcanic rocks (73), provide an appropriate terrestrial analog to an ancient Lake Gale and the Murray formation. Sedimentary units in core T-A95 from that lake include both fine-grained clastic sediments and coarser-grained dacite−rhyolite air-fall tephra. The highest combined abundance of tridymite plus cristobalite (up to >30% with no quartz) are in unit IIIa, a silty sand clastic sediment with ∼60 wt.% SiO_2. Tridymite and cristobalite are present at generally lower abundances (5–30%) in two air-fall tephra layers in unit IIIb (∼70 wt.% SiO_2) from Plinian eruptions 8–60 km away (73). The Lake Tecocomulco analog shows that sediments with high abundances of tridymite and cristobalite, like those in the Buckskin sample, are obtainable in lake sediments with a catchment that includes silicic volcanism.

By partial analogy with tridymite-bearing sediments in Lake Tecocomulco (73), silicic volcanic rocks exposed within the catchment of ancient Lake Gale could have contributed the detrital tridymite and cogenetic material to the Murray formation. Fine-grained sediments are most readily formed by downstream fining in alluvial settings, and evidence for this is preserved in the Gale crater moat (74). The even and fine lamination observed in the Murray formation at Marias Pass is inconsistent with direct fallout of distal volcanic ash, even through a water column (1). For the lower Murray formation at Pahrump Hills, these regular laminae were interpreted to result from the settling of fines derived from distal deltas, likely as plumes (1). Therefore, we suggest that the tridymite-bearing material was derived by erosion and transport from a silicic source area in a manner similar to Lake Tecocomulco. Unlike the Lake Tecocomulco analog, which has units of interstratified silicic volcanic ash (73), there are no known silicic volcanic rocks interstratified with Gale sedimentary rocks, so we appeal to crater rim and central peak regions as sources of tridymite-bearing material that may predate the Gale crater impact.

Recent studies have suggested that the Gale crater rim/wall may host igneous lithologies more evolved than other known martian igneous rocks, ranging up to ∼67 wt.% SiO_2 (75). The Lake Gale basin would have captured sediments from these terrains. Mineralogical observations across Mars made by orbital remote sensing have also

been interpreted as evidence for magma evolution to compositions more silicic than basaltic (76–78). The microclast in the ureilite meteorite EET 87720, which has a Buckskin-like mineralogy and composition, is also consistent with an evolved magma on a parent body that is possibly Mars (58).

The mixed-cation salts, minor oxides, and any precipitated silica in Buckskin amorphous material can be interpreted as cements precipitated during deposition and/or from later infiltrations by aqueous solutions having variable chemistries, temperatures, and acidities. The crystalline cation-deficient magnetite could also be present as a primary precipitate and cement, but there are insufficient constraints available to exclude igneous detritus or diagenesis of Fe-bearing materials. Anhydrite is interpreted as late fracture and vein fill as reported for other drill samples (8), implying its precipitation postdates lithification of the tridymite-bearing sedimentary rock.

The origin of the opal-A is not constrained. It could have formed as an alteration product of high-SiO_2 volcanic glass, as a residue from acid sulfate leaching of silicates in the sediment source region, or as similar residue from leaching in the sediment itself. Another alternative is primary precipitation of silica gel in the Gale lake environment followed by diagenesis to opal-A and opal-CT after burial. CheMin would not be able to distinguish between silica gel and opal-A, however (*SI Appendix*, Fig. S6). At present, there are insufficient constraints to partition the high-SiO_2 amorphous material among the aforementioned possible formation pathways, although silicic volcanism and diagenesis can account for all opal-A and opal-CT.

Implications for Martian Petrogenesis

The Buckskin tridymitic mudstone sample contains abundant SiO_2 phases (∼55 wt.% of bulk sample) consisting of 14 wt.% tridymite, 2 wt.% cristobalite, 6 wt.% opal-CT, 33 wt.% opal-A and/or high-SiO_2 glass, and no quartz. The monoclinic tridymite is well crystallized and not a mineraloid, such as opal with partial tridymite stacking, which might be attributed to a low-temperature origin. Because the martian crust is largely basaltic, we explored other options for the origin of Buckskin tridymite. Of all of the options, derivation from silicic volcanic rocks is the most parsimonious within available constraints, the most important being its high formation temperature (∼870 °C to ∼1,470 °C).

Although the general view of Mars is that of a basaltic planet, tridymite at Buckskin adds support to previous studies that describe regions of Mars where occurrences of high-SiO_2 igneous rocks have been inferred (76–78). Furthermore, the Buckskin tridymitic mudstone is yet another indication of evolved volcanic compositions in sedimentary source regions of Gale crater (75). The unexpected discovery of tridymite at Gale crater is further evidence of the complexity of igneous petrogenesis on Mars, with igneous evolution to high-silica compositions.

1. Grotzinger JP, et al. (2015) Deposition, exhumation, and paleoclimate of an ancient lake deposit, Gale crater, Mars. *Science* 350(6257):aac7575.
2. Rampe EB, et al. (2016) Diagenesis in the Murray Formation, Gale Crater, Mars. *Lunar Planet Sci* 47:Abstr 2543.
3. Grotzinger JP, et al. (2012) Mars Science Laboratory mission and science investigation. *Space Sci Rev* 170(1-4):5–56.
4. Blake D, et al. (2012) Characterization and calibration of the CheMin mineralogical instrument on Mars Science Laboratory. *Space Sci Rev* 170(1):341–399.
5. Lafuente B, Downs RT, Yang H, Stone N (2015) The power of databases: The RRUFF project. *Highlights in Mineralogical Crystallography*, eds Armbruster T, Danisi RM (De Gruyter, Berlin), pp 1–30.
6. Chipera SJ, Bish DL (2002) FULLPAT: A full-pattern quantitative analysis program for x-ray powder diffraction using measured and calculated patterns. *J Appl Cryst* 35:744–749.
7. Bish DL, et al.; MSL Science Team (2013) X-ray diffraction results from Mars Science Laboratory: Mineralogy of Rocknest at Gale crater. *Science* 341(6153):1238932.
8. Vaniman DT, et al.; MSL Science Team (2014) Mineralogy of a mudstone at Yellowknife Bay, Gale crater, Mars. *Science* 343(6169):1243480.
9. Treiman AH, et al. (2016) Mineralogy, provenance, and diagenesis of a potassic basaltic sandstone on Mars: CheMin X-ray diffraction of the Windjana sample (Kimberley area, Gale Crater). *J Geophys Res Planets* 121(1):75–106.
10. Graetsch H, Topalovic-Dierdorf I (1996) ^{29}Si MAS NMR spectrum and superstructure of modulated tridymite L3-To(MX-1). *Eur J Mineral* 8(1):103–113.

11. Elzea JM, Odom IE, Miles WJ (1994) Distinguishing well ordered opal-CT and opal-C from high temperature cristobalite by X-ray diffraction. *Anal Chim Acta* 286(1):107–116.

12. Eversull LG, Ferrell RE (2008) Disordered silica with tridymite-like structure in the Twiggs clay. *Am Mineral* 93(4):565–572.

13. Mason B (1953) Tridymite and christensenite. *Am Mineral* 38(9-10):866–867.

14. Grant RW (1967) New data on tridymite. *Am Mineral* 52(3-4):536.

15. Papike JJ, Karner JM, Shearer CK, Burger PV (2009) Silicate mineralogy of martian meteorites. *Geochim Cosmochim Acta* 73(24):7443–7485.

16. Swamy V, Saxena SK, Sundman B, Zhang J (1994) A thermodynamic assessment of silica phase diagram. *J Geophys Res Solid Earth* 99(B6):11787–11794.

17. Koike CR, et al. (2013) Infrared spectra of silica polymorphs and the conditions of their formation. *Astrophys J* 778(1):60.

18. Holmquist S (1961) Conversion of quartz to tridymite. *J Am Ceram Soc* 44(2):82–86.

19. Sato M (1963) X-ray study of tridymite (1). *Mineral J* 4(2):115–130.

20. Sato M (1963) X-ray study of low tridymite (2). *Mineral J* 4(2):131–146.

21. Nukui A, Nakazawa H, Akao M (1978) Thermal changes in monoclinic tridymite. *Am Mineral* 63(11-12):1252–1259.

22. Carpenter MA, Wennemer M (1985) Characterization of synthetic tridymites by transmission electron microscopy. *Am Mineral* 70(5-6):517–528.

23. Garofalini SH, Miller AD (1986) Kinetics of tridymite formation. *J Cryst Growth* 78(1):85–96.

24. Fabian D, Jäger C, Henning T, Dorschner J, Mutschke H (2000) Steps toward interstellar silicate mineralogy. V. Thermal evolution of amorphous magnesium silicates and silica. *Astron Astrophys* 364:282–292.

25. Chen S, Jak E, Hayes PC (2005) Phase equilibria in the cristobalite, tridymite and py-roxene primary phase fields in the MgO-"FeO"-SiO₂ system in equilibrium with me-tallic iron. *ISIJ Int* 45(6):791–797.

26. Hirose T, Kihara K, Okuno M, Fujinami S, Shinoda K (2005) X-ray, DTA and Raman studies of monoclinic tridymite and its higher temperature orthorhombic modifica-tion with varying temperature. *J Mineral Petrol Sci* 100(2):55–69.

27. Dapiaggi M, et al. (2015) The formation of silica high temperature polymorphs from quartz: Influence of grain size and mineralising agents. *J Eur Ceram Soc* 35(16):4547–4555.

28. Ross CS, Smith RL (1961) *Ash Flow Tuffs: Their Origin, Geologic Relations and Iden-tification*, USGS Professional Paper (US Geol Surv, Boulder, CO), Vol 366.

29. Keith TE, Muffler L (1978) Minerals produced during cooling and hydrothermal al-teration of ash flow tuff from Yellowstone drill hole Y-5. *J Volcanol Geotherm Res* 3(3):373–402.

30. Broxton DE, Heiken GH, Chipera S, Byers FM, Jr (1995) Stratigraphy, petrography, and mineralogy of Bandelier Tuff and Cerro Toledo deposits. *Earth Science Investigations for Environmental Restoration—Los Alamos National Laboratory, Technical Area 21*, eds Broxton DE, Eller GG (Los Alamos Natl Lab, Los Alamos, NM), Rep LA-12934-MS, pp 33–63.

31. Streck M, Grunder A (1995) Crystallization and welding variations in a widespread ignimbrite sheet; the Rattlesnake Tuff, eastern Oregon, USA. *Bull Volcanol* 57(3):151–169.

32. Bargar KE, Keith TE (1999) *Hydrothermal Mineralogy of Core from Geothermal Drill Holes at Newberry Volcano, Oregon*, USGS Professional Paper (US Geol Surv, Boulder, CO), Vol 1578.

33. Chigira M, Nakamoto M, Nakata E (2002) Weathering mechanisms and their effects on the landsliding of ignimbrite subject to vapor-phase crystallization in the Shir-akawa pyroclastic flow, northern Japan. *Eng Geol* 66(1):111–125.

34. Breitkreuz C (2013) Spherulites and lithophysae—200 years of investigation on high-temperature crystallization domains in silica-rich volcanic rocks. *Bull Volcanol* 75(4):1–16.

35. Galan LDP, Doval M, La Iglesia A, Soriano J, Chavez L (2013) Occurrence of silica polymorphs nanocrystals in tuffaceous rocks, Province of the Mesa Central, Mexico, and their formation from subcritical Si-rich fluids. *Am Mineral* 98(5-6):977–985.

36. Martin AM, et al. (2015) Fayalite oxidation processes in Obsidian Cliffs rhyolite flow, Oregon. *Am Mineral* 100(5-6):1153–1164.

37. Hamasaki S (2002) Volcanic-related alteration and geochemistry of Iwodake volcano, Satsuma-Iwojima, Kyushu, SW Japan. *Earth Planets Space* 54(3):217–229.

38. Shinohara H, Kazahaya K, Saito G, Matsushima N, Kawanabe Y (2002) Degassing activity from Iwodake rhyolitic cone, Satsuma-Iwojima volcano, Japan: Formation of a new degassing vent, 1990–1999. *Earth Planets Space* 54(3):175–185.

39. Kazahaya K, Shinohara H, Saito G (2002) Degassing process of Satsuma-Iwojima vol-cano, Japan: Supply of volatile components from a deep magma chamber. *Earth Planets Space* 54(3):327–335.

40. Matsushima N, Kazahaya K, Saito G, Shinohara H (2003) Mass and heat flux of vol-canic gas discharging from the summit crater of Iwodake volcano, Satsuma-Iwojima, Japan, during 1996–1999. *J Volcanol Geotherm Res* 126(3):285–301.

41. Baxter PJ, et al. (1999) Cristobalite in volcanic ash of the Soufriere Hills volcano, Montserrat, British West Indies. *Science* 283(5405):1142–1145.

42. Del Moro S, Renzulli A, Tribaudino M (2011) Pyrometamorphic processes at the magma–hydrothermal system interface of active volcanoes: Evidence from buchite ejecta of Stromboli (Aeolian Islands, Italy). *J Petrol* 52(3):541–564.

43. Getahun A, Reed MH, Symonds R (1996) Mount St. Augustine volcano fumarole wall rock alteration: Mineralogy, zoning, composition and numerical models of its for-mation process. *J Volcanol Geotherm Res* 71(2):73–107.

44. Wager L, Weedon D, Vincent E (1953) A granophyre from Coire Uaigneich, Isle of Skye, containing quartz paramorphs after tridymite. *Mineral Mag* 30(223):263–275.

45. Black GP (1954) The significance of tridymite in igneous and metamorphic petro-genesis. *Mineral Mag* 30(227):518–524.

46. Holness MB (2002) Spherulitic textures formed during crystallization of partially melted arkose, Rum, Scotland. *Geol Mag* 139(06):651–663.

47. Whitehead J, Grieve RAF, Spray JG (2002) Mineralogy and petrology of melt rocks from the Popigai impact structure, Siberia. *Meteorit Planet Sci* 37(5):623–647.

48. Jackson JC, Horton JW, Chou I-M, Belkin HE (2011) Monoclinic tridymite in clast-rich impact melt rock from the Chesapeake Bay impact structure. *Am Mineral* 96(1):81–88.

49. Schwenzer SP, et al. (2012) Gale Crater: Formation and post-impact hydrous envi-ronments. *Planet Space Sci* 70(1):84–95.

50. Bridges J, et al. (1995) Cristobalite- and tridymite-bearing clasts in Parnallee (LL3) and Farmington (L5). *Meteoritics* 30(6):715–727.

51. Xirouchakis D, Draper DS, Schwandt CS, Lanzirotti A (2002) Crystallization conditions of Los Angeles, a basaltic Martian meteorite. *Geochim Cosmochim Acta* 66(10):1867–1880.

52. Treiman AH, Lanzirotti A, Xirouchakis D (2004) Ancient water on asteroid 4 Vesta: Evidence from a quartz veinlet in the Serra de Magé eucrite meteorite. *Earth Planet Sci Lett* 219(3-4):189–199.

53. Imae N, Ikeda Y, Kojima H (2005) Petrology of the Yamato nakhlites. *Meteorit Planet Sci* 40(11):1581–1598.

54. Hezel DC, Palme H, Nasdala L, Brenker FE (2006) Origin of SiO₂-rich components in ordinary chondrites. *Geochim Cosmochim Acta* 70(6):1548–1564.

55. Schrader DL, et al. (2010) Sulfide-rich metallic impact melts from chondritic parent bodies. *Meteorit Planet Sci* 45(5):743–758.

56. Bonin B (2012) Extra-terrestrial igneous granites and related rocks: A review of their occurrence and petrogenesis. *Lithos* 153:3–24.

57. Seddio SM, Korotev RL, Jolliff BL, Wang A (2015) Silica polymorphs in lunar granite: Implications for granite petrogenesis on the Moon. *Am Mineral* 100(7):1533–1543.

58. Beard AD, Downes H, Chaussidon M (2015) Petrology of a nonindigenous micro-granitic clast in polymict ureilite EET 87720: Evidence for formation of evolved melt on an unknown parent body. *Meteorit Planet Sci* 50(9):1613–1623.

59. Leroux H, Cordier P (2006) Magmatic cristobalite and quartz in the NWA 856 Martian meteorite. *Meteorit Planet Sci* 41(6):913–923.

60. Ren S, et al. (2008) The preparation of tridymite crystal by chemical processing. *Phase Transit* 81(5):395–402.

61. Herdianita NR, Browne PRL, Rodgers KA, Campbell KA (2000) Mineralogical and textural changes accompanying ageing of silica sinter. *Miner Deposita* 35(1):48–62.

62. Campbell KA, Sannazzaro K, Rodgers K, Herdianita N, Browne P (2001) Sedimentary facies and mineralogy of the late Pleistocene Umukuri silica sinter, Taupo Volcanic Zone, New Zealand. *J Sediment Res* 71(5):727–746.

63. Rodgers KA, et al. (2004) Silica phases in sinters and residues from geothermal fields of New Zealand. *Earth Sci Rev* 66(1-2):1–61.

64. Lynne BY, Campbell KA, Moore JN, Browne PRL (2005) Diagenesis of 1900-year-old siliceous sinter (opal-A to quartz) at Opal Mound, Roosevelt Hot Springs, Utah, U.S.A. *Sediment Geol* 179(3-4):249–278.

65. Lynne BY, Campbell KA, Perry RS, Browne P, Moore J (2006) Acceleration of sinter diagenesis in an active fumarole, Taupo Volcanic Zone, New Zealand. *Geology* 34(9):749–752.

66. Channing A, Butler IB (2007) Cryogenic opal-A deposition from Yellowstone hot springs. *Earth Planet Sci Lett* 257(1):121–131.

67. Garcia-Valles M, Fernandez-Turiel J, Gimeno-Torrente D, Saavedra-Alonso J, Marti-nez-Manent S (2008) Mineralogical characterization of silica sinters from the El Tatio geothermal field, Chile. *Am Mineral* 93(8-9):1373–1383.

68. Preston LJ, Benedix GK, Genge MJ, Sephton MA (2008) A multidisciplinary study of silica sinter deposits with applications to silica identification and detection of fossil life on Mars. *Icarus* 198(2):331–350.

69. Rodgers KA, Cook KL, Browne PRL, Campbell KA (2002) The mineralogy, texture and significance of silica derived from alteration by steam condensate in three New Zealand geothermal fields. *Clay Miner* 37(2):299–322.

70. Saishu H, Okamoto A, Tsuchiya N (2012) Mineralogical variation of silica induced by Al and Na in hydrothermal solutions. *Am Mineral* 97(11-12):2060–2063.

71. Ramseyer K, et al. (2013) Primary silica precipitate at the Precambrian/Cambrian boundary in the south Oman salt basin, sultanate of Oman. *Mar Pet Geol* 39(1):187–197.

72. Al Rajaibi IM, Hollis C, Macquaker JH (2015) Origin and variability of a terminal Proterozoic primary silica precipitate, Athel Silicilyte, South Oman Salt Basin, Sul-tanate of Oman. *Sedimentology* 62(3):793–825.

73. Roy PD, Caballero M, Lozano R, Pi T, Morton O (2009) Late Pleistocene-Holocene geochemical history inferred from Lake Tecocomulco sediments, Basin of Mexico, Mexico. *Geochem J* 43(1):49–64.

74. Szabó T, Domokos G, Grotzinger JP, Jerolmack DJ (2015) Reconstructing the transport history of pebbles on Mars. *Nat Commun* 6:8366.

75. Sautter V, et al. (2015) *In situ* evidence for continental crust on early Mars. *Nat Geosci* 8:605–609.

76. Christensen PR, et al. (2005) Evidence for magmatic evolution and diversity on Mars from infrared observations. *Nature* 436(7050):504–509.

77. Smith MR, Bandfield JL (2012) Geology of quartz and hydrated silica-bearing deposits near Antoniadi Crater, Mars. *J Geophys Res Planets* 117(E6):E06007.

78. Wray JJ, et al. (2013) Prolonged magmatic activity on Mars inferred from the de-tection of felsic rocks. *Nat Geosci* 6(12):1013–1017.